

Slip-System-Related Dislocation Study from *In-Situ* Neutron Measurements

E-WEN HUANG, ROZALIYA BARABASH, NAN JIA, YAN-DONG WANG,
GENE E. ICE, BJØRN CLAUSEN, J. HORTON, and PETER K. LIAW

A combined experimental/computational approach is employed to study slip-system-related dislocation-substructure formation during uniaxial tension of a single-phase, face-centered-cubic (fcc), nickel-based alloy. *In-situ* neutron-diffraction measurements were conducted to monitor the peak-intensity, peak-position, and peak-broadening evolution during a displacement-controlled, monotonic-tension experiment at room temperature. The measured lattice-strain evolution and the macrostress/macrostrain curves were used to obtain the material parameters required for simulating the texture development by a visco-plastic self-consistent (VPSC) model. The simulated texture compared favorably with experimentally-determined texture results over a range of 0 to 30 pct engineering strain. The grain-orientation-dependent input into the Debye-intensity ring was considered. Grains favorably oriented relative to the two detector banks in the geometry of the neutron experiment were indicated. For the favorably oriented grains, the simulated slip-system activity was used to calculate the slip-system-dependent, dislocation-contrast factor. The combination of the calculated contrast factor with the experimentally-measured peak broadening allows the assessment of the parameters of the dislocation arrangement within the specifically oriented grains, which has a quantitative agreement with the transmission-electron-microscopy results.

DOI: 10.1007/s11661-008-9704-1

© The Minerals, Metals & Materials Society and ASM International 2008

I. INTRODUCTION

IN polycrystalline materials, mechanical properties are related to textures, especially under plastic deformation: Slip on specific crystallographic planes during the plastic deformation may produce lattice rotations and, hence, develop texture. However, Heidebach comments that it is not a trivial job to reveal the plastic flow,

considering the texture development with the microstructure evolution.^[1,2] Hill's^[3] and Hutchinson's^[4] self-consistent (SC) models have been applied very successfully to simulate the micromechanical behavior of polycrystalline materials^[5] by the lattice-strain evolution based on neutron-diffraction measurements *via* the elasto-plastic self-consistent (EPSC) model for several metallic materials.^[6,7] The intrinsic assumptions of the EPSC model consider the active inelastic-deformation mechanisms, and, hence, the stiffness/compliance constants are important for simulations.^[8–10] The present study extends SC modeling to moderate-to-large deformation strains, considering the grain rotation for describing preferred grain-orientation distributions. In the current work, a visco-plastic self-consistent (VPSC) model is applied to simulate the texture development, based on the measured lattice strains and macrostress-macrostrain responses from a nickel-based alloy. The VPSC model considers the activity of slip systems and its influence on grain rotation.^[11] The VPSC code used in this study is based on previous work.^[12–14] Experimental macro/lattice stress-strain curves are used as an input to simulate the texture and the probability of the active-slip systems from the multiple *hkl* reflections. Moreover, a peak-width analysis is applied to combine the texture-evolution information for the slip-system-dependent, dislocation-contrast factor. The peak profiles are measured at a time-of-flight (TOF) neutron-diffraction instrument. The contrast factors are used to determine the direction of the active dislocations moving on the slip planes, relative to the specimen-coordinate system of the instrumental environment. This demonstration as *in-situ*

E-WEN HUANG, Graduate Student, and PETER K. LIAW, Professor and Ivan Racheff Chair of Excellence, are with the Materials Science and Engineering Department, University of Tennessee, Knoxville, TN 37996. ROZALIYA BARABASH, Research Professor, is with the Materials Science and Technology Division, Oak Ridge National Laboratory, Oak Ridge, TN 37831, and the Center for Materials Processing, University of Tennessee. Contact e-mail: barabashr@ornl.gov NAN JIA, Lecturer, is with the Key Laboratory for Anisotropy and Texture of Materials, Ministry of Education, Northeastern University, Shenyang 110004, P.R. China. YAN-DONG WANG, Professor, is with the Materials Science and Engineering Department, University of Tennessee, and Key Laboratory for Anisotropy and Texture of Materials, Ministry of Education, Northeastern University. GENE E. ICE, Group Leader, X-ray Scattering and Microscopy Group, and J. HORTON, Senior Researcher, Alloying Behavior and Design Group, are with the Materials Science and Technology Division, Oak Ridge National Laboratory. BJØRN CLAUSEN, Technical Staff Member and SMARTS Instruments Scientist, is with the Los Alamos Neutron Science Center, Los Alamos National Laboratory, Los Alamos, NM 87545.

This article is based on a presentation given in the symposium entitled "Neutron and X-Ray Studies for Probing Materials Behavior," which occurred during the TMS Spring Meeting in New Orleans, LA, March 9–13, 2008, under the auspices of the National Science Foundation, TMS, the TMS Structural Materials Division, and the TMS Advanced Characterization, Testing, and Simulation Committee.

Article published online November 4, 2008

experiment offers new insights about evolving dislocation arrangements and serves as a reference for further dislocation investigations.

II. EXPERIMENTAL PROCEDURE

A. Materials and In-Situ Neutron Experiments

The HASTELLOY C-22HS,* a nickel-based alloy

*HASTELLOY C-22HS is a trademark of Haynes International Inc., Kokomo, IN

(Ni-21Cr-17Mo, in wt pct) was selected as the sample material. The alloy was annealed to dissolve most precipitates and showed a texture-free condition from previous neutron-diffraction measurements^[15] in axial and transverse directions. The average starting grain size was about 90 μm , and the texture-free condition made the alloy a good specimen to interpret peak-refinement results: There were no initial texture and second-phase precipitates. A transmission electron microscopy (TEM) study confirmed that the alloy had a single-phase face-centered-cubic (fcc) structure.^[16] The room-temperature, *in-situ* neutron measurements were conducted with the spectrometer for materials research at temperature and stress (SMARTS)^[17] beamline of the Los Alamos Neutron Science Center (LANSCE). The gage volume was 120 mm³ for the measurements of the monotonic tension. The strain rate was 0.001 per second.

B. Neutron-Data Analyses

The neutron-diffraction profiles were refined by the general structure analysis system (GSAS)^[18] for investigating the peak position, intensity, peak profiles, and width, respectively. A pseudo-Voigt function (GSAS function 3) was fit to the data and used to distinguish different sources of peak broadening.

The refined peak positions of each hkl were calculated during the evolution of lattice strain (ε_{hkl}), based on the change in the d spacing (d_{hkl}) as a function of the stress, relative to the initial d spacing (d_{hkl}^0), as shown in Eq. [1]:

$$\varepsilon_{hkl} = \frac{d_{hkl} - d_{hkl}^0}{d_{hkl}^0} \quad [1]$$

The lattice-strain evolution was used as an input for fitting the compliance within the elastic region, for the VPSC simulations.

The peak intensity was fitted for the individual hkl peaks. The normalized intensity evolution as a function of stress was calculated using Eq. [2] to monitor the texture development through the tensile test, which was further used to compare with the VPSC-simulated texture development.

$$I_{hkl} = \frac{I_{hkl}^{\text{deformed}}}{I_{hkl}^0} \quad [2]$$

The peak width was decomposed into the Gaussian and Lorentzian broadening components as a full-width half-maximum (FWHM). The profile-shape functions used in profile fitting programs are shown in Eqs. [3] and [4] for Gaussian and Lorentzian.

$$G = I_0 \exp \left(-\ln 2 \left(\frac{2\Theta - 2\Theta_0}{w} \right)^2 \right) \quad [3]$$

$$L = I_0 \left(1 + \left(\frac{2\Theta - 2\Theta_0}{w} \right)^2 \right)^{-1} \quad [4]$$

Here, I_0 is peak intensity, w is half FWHM, and 2Θ is the peak position.

C. Model of Dislocation Arrangement

We assume the formation of a hierarchical dislocation structure in the plastically-deformed material when some part of dislocations group within dislocation walls and some part remain randomly distributed. The formation of the hierarchical dislocation structure in many metallic polycrystalline materials under different deformation has been previously reported.^[2,19–26] In our work, the formation of the hierarchical dislocation structures is considered, which is similar to References 24 through 26. These microstructures mainly are dislocation walls, which create certain misorientation/tilt/twist between the neighboring regions. Note that there are also partial randomly-distributed dislocations populated between the dislocation walls in the same grain. There is practically no misorientation/tilt/twist in the interior of the walls. For simplicity, we assume that the dislocation walls are composed from the equidistant edge dislocations, and screw dislocations remain randomly distributed in the cell interior, as shown in Figure 1. As was presented previously,^[26–30] equidistant-dislocation walls result in the Lorentzian type of broadening. The randomly distributed or weakly correlated dislocations in the interior yield the Gaussian type of broadening.^[19,20,27] Further details on the model and calculations are described in Section III–D.

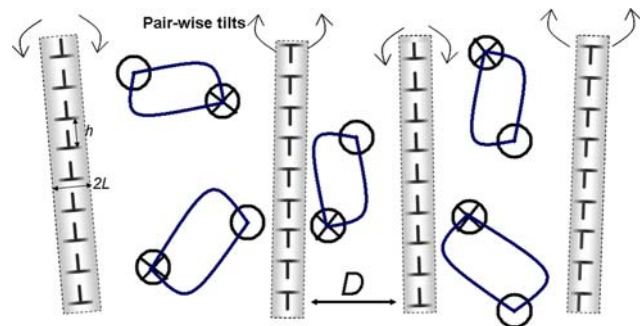


Fig. 1—Sketch of the patterned-dislocation structure with dislocation walls and the randomly distributed dislocations. Each wall creates the pairwise tilt between two adjacent regions. The shadowed regions near each wall indicate the area in the immediate vicinity of the equidistant-dislocation wall ($L < h$), where strain field from dislocations within the wall are significant.

D. Transmission Electron Microscopy

Complementary TEM analysis was performed at 200 kV in a TECHNAI 20 electron microscope. Samples for TEM were prepared from a slice cut at 45 deg to the loading direction to maximize the parts of having the slip plane parallel to the surface of the TEM sample.

III. EXPERIMENTAL RESULTS

A. Tensile Tests and Fitting Parameters for Simulations

The 0.2 pct yield strength of the alloy is about 370 MPa. Lattice-strain vs stress curves for hkl s, $\{111\}$, $\{200\}$, $\{220\}$, $\{311\}$, $\{331\}$, $\{420\}$, and $\{422\}$, in loading and transverse directions are shown in Figures 2(a) and (b), respectively. The measurements made at 20, 30, 40, 50, 60, 70, 80, 90, 110, and 120 MPa are used to calculate the compliance of the materials for texture simulations. The linearity of the different lattice strain (ϵ_{hkl}) vs stress curves shown in Figure 2 suggests that the alloy intrinsically follows a generalized Hooke's law,^[31] with $\{111\}$, the stiffest plane,^[31] and $\{200\}$, the least stiff plane^[31] within the elastic region (up to 120 MPa).

B. VPSC Simulation

A VPSC model was implemented for estimating the distribution of microstresses and texture evolution for the alloy. The SC approach developed by Hutchinson^[32] was used here with an extension of the Eshelby inclusion tensor to macroscopically anisotropic materials.^[33] In the model, a total number of 2592 grains were simulated through the VPSC model.^[34] The lattice-strain (ϵ_{hkl}) distribution was simulated at different loading levels. The grains used for modeling are based on the

microstructural characteristics obtained from the neutron-diffraction data. The lattice-strain (ϵ_{hkl}) distribution was simulated at different loading levels. For simplicity, only grain-to-grain interactions existing within the respective phase and the influence of texture on the plastic deformation were considered. The method applied determined the stress needed to give a strain field at each loading level. The strain field was simulated to match the measured lattice-strain distribution for each load. An empirical Voce-hardening rule (Eq. [5]) was used in the simulation to describe the critical resolved shear stress (CRSS) evolution of individual deformation modes:

$$\tau = \tau_0 + (\tau_0 + \theta_1 \Gamma) \{1 - \exp(-\theta_0 \Gamma / \tau_1)\} \quad [5]$$

Here, τ is the instantaneous flow stress; τ_0 and $\tau_0 + \tau_1$ are the initial and final back-extrapolated CRSS, respectively; θ_0 and θ_1 are the initial and asymptotic hardening rates; and Γ is the accumulated plastic shear in the grain. All the parameters were derived by fitting the model to the experimental neutron measurements of different $\{hkl\}$ lattice-strain evolution and to the laboratory macroscopic stress-strain curve of the material.^[35]

The compliances used in the simulations were fitted to the measured lattice strain (ϵ_{hkl}) at different load levels within 120 MPa, in the elastic region. Since the studied material has an fcc structure, 18 cubic slip systems^[36] of $\{111\}\langle 110 \rangle$ type were considered, as shown in Table I. The critical resolved stress and the hardening parameter for different slip systems and the elastic constants used in the simulation of this alloy are listed in Table II. In Figure 3, the uniaxial monotonic-tensile experiments are presented as a stress-strain curve in open symbols, and the VPSC simulations are shown in a solid line. The simulations agree with the measurements in both the elastic and the plastic regions. The onset of the plastic

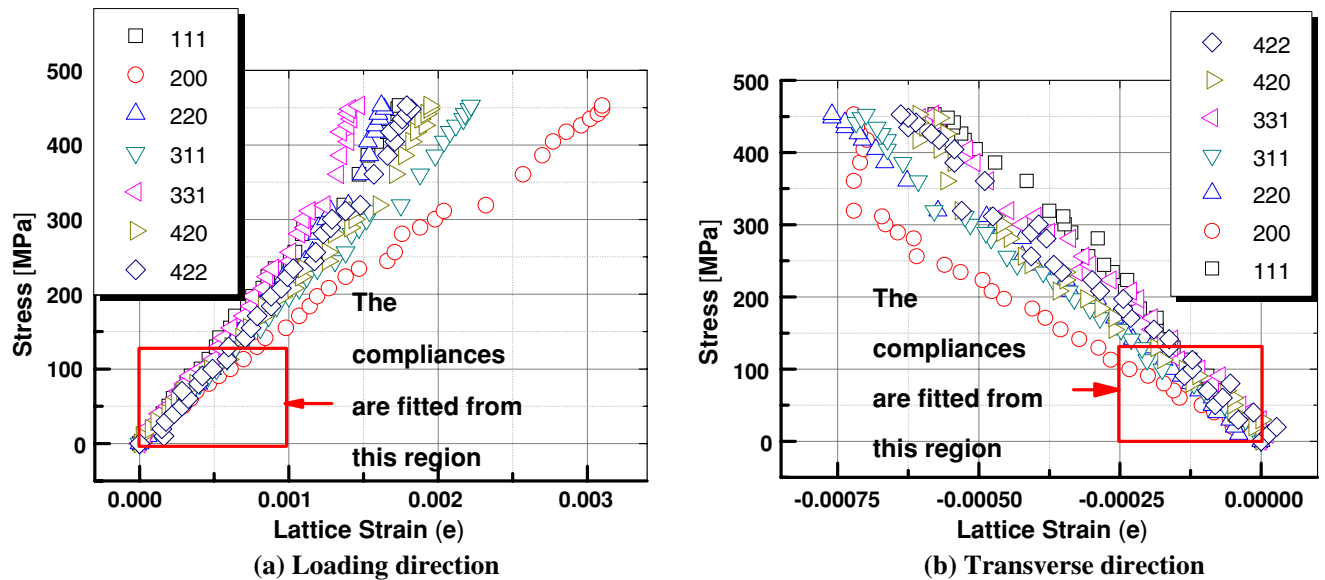


Fig. 2—Lattice-strain stress curves of hkl 111, 200, 220, 311, 331, 420, and 422. The linearity starts to deviate about 370 MPa, corresponding to the 0.2 pct yield strength: (a) loading and (b) transverse directions.

Table I. Slip System Considered in the Current Study

Edge Dislocation Slip system	Slip Plane			Burgers Vector		
	<i>h</i>	<i>k</i>	<i>l</i>	<i>u</i>	<i>v</i>	<i>w</i>
1	1	1	1	1	$\bar{1}$	0
2	1	1	1	0	1	$\bar{1}$
3	$\bar{1}$	1	1	1	0	$\bar{1}$
4	$\bar{1}$	1	1	1	1	0
5	$\bar{1}$	1	1	0	1	$\bar{1}$
6	$\bar{1}$	1	1	1	0	1
7	1	1	$\bar{1}$	1	$\bar{1}$	0
8	1	1	$\bar{1}$	0	1	1
9	1	1	$\bar{1}$	1	0	1
10	1	$\bar{1}$	1	1	1	0
11	1	$\bar{1}$	1	1	0	$\bar{1}$
12	1	$\bar{1}$	1	0	1	1

Screw Dislocation Slip system	Dislocation Line			Burgers Vector		
	τ_x	τ_y	τ_z	<i>u</i>	<i>v</i>	<i>w</i>
1	1	$\bar{1}$	0	1	$\bar{1}$	0
2	0	1	$\bar{1}$	0	1	$\bar{1}$
3	1	0	$\bar{1}$	1	0	$\bar{1}$
4	1	1	0	1	1	0
5	1	0	1	1	0	1
6	0	1	1	0	1	1

Table II. Material Parameters Used in VPSC Simulations for the Alloy: *Q* Denotes the Thermal Expansion Coefficient; τ_0 and θ_1 are the Critical Resolved Stress and the Hardening Parameter, Respectively; and *C*₁₁, *C*₁₂, and *C*₄₄ Are the Single-Crystal Elastic Constants

<i>Q</i> ($\times 10^{-6}$)	τ (MPa)	θ (MPa)	Single Crystal Elastic Constants (GPa)		
			<i>C</i> ₁₁	<i>C</i> ₁₂	<i>C</i> ₄₄
18	135	450	303.0	210.0	106.0

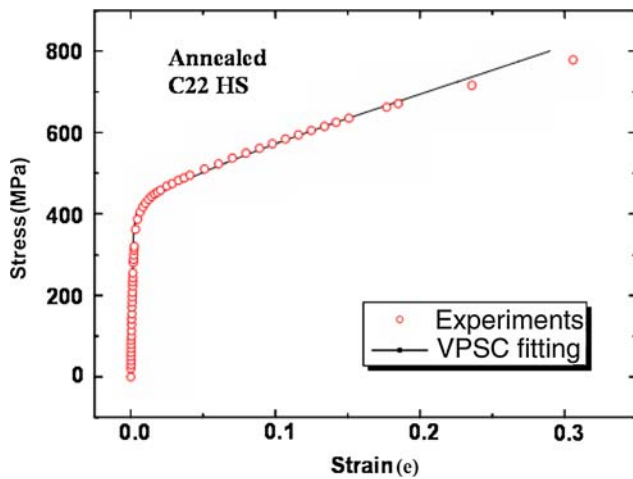


Fig. 3—Stress-strain curve of the alloy for a monotonic-tension experiment. The measurements are depicted in open symbols and VPSC fitting is in a solid line.

deformation (370 MPa) is fitted, too. The simulated inverse-pole figures along the loading direction are plotted in Figure 4. Figure 4(a) demonstrates that the initial texture is practically random. Figure 4(b) shows the VPSC simulated texture under the large plastic deformation at 825 MPa using the measured random texture as the input. The simulated results show a preferred texture in {100} and {111} poles, but not in the {110} pole.

C. In-Situ Neutron Measurements

To further compare the simulations and experiments, the measured *in-situ* neutron experimental data along the loading direction were used, as shown in Figure 5(a). The results are normalized with respect to the intensity at the undeformed status, as calculated by Eq. [2]. The intensity evolution demonstrates that the texture gradually develops as the material plastically deforms. The intensity does not vary before the 0.2 pct yield strength of about 370 MPa. When the tensile stress reaches 825 MPa, the intensity of the {111} peak increases more than 1.5 times, compared to the undeformed state. The {200} peak intensity increases by a factor of ~1.5. The {311} has the smallest deviation, and the intensity decreases about 20 pct, while the {220} almost disappears. These measured, intensity-evolution results demonstrate that {111} and {200} gradually develop the texture along the loading direction as open squares in Figure 5(b), but {220} intensity disappears from the loading direction. Similar trends are reported from other fcc polycrystalline alloys^[37] and the effect of grain orientation on the deformation structure in cold-rolled polycrystalline.^[38] The VPSC-simulated results on {111} and {100} at 825 MPa are presented in Figure 5(b) as open circles. The simulated texture of both {111} and {100} increases in the simulation and there is a stronger {111} texture component than {100}. As a result, there is a qualitative agreement between the simulations and the *in-situ* neutron measurement.

However, the amplitude of the simulated texture is larger than the measured one at 825 MPa. In Figure 5(b), the measured {111} texture increases 1.5 times, while the simulated one rises 3 times. The same difference is seen in the {200} texture: The measured intensity rises about 0.5 times and the simulated enlarges almost 1.5 times. The discrepancy between the simulated and the measured intensities shows an overestimation in texture simulation. The overestimation indicates that work hardening should be considered with the microstructure evolution, as discussed in Section D.

D. Microstructure-Evolution Estimation via Peak-Profile Analyses

Work hardening, which relates to the flow stress, was first derived by Taylor^[39] to link the microstructure evolution to material-mechanical properties under plastic deformation. Our analysis of the microstructure evolution during the deformation is based on peak broadening observed from the *in-situ* neutron measurements (Figure 6). The mechanically-induced stored

The VPSC-simulated, inverse-pole figures along the loading direction

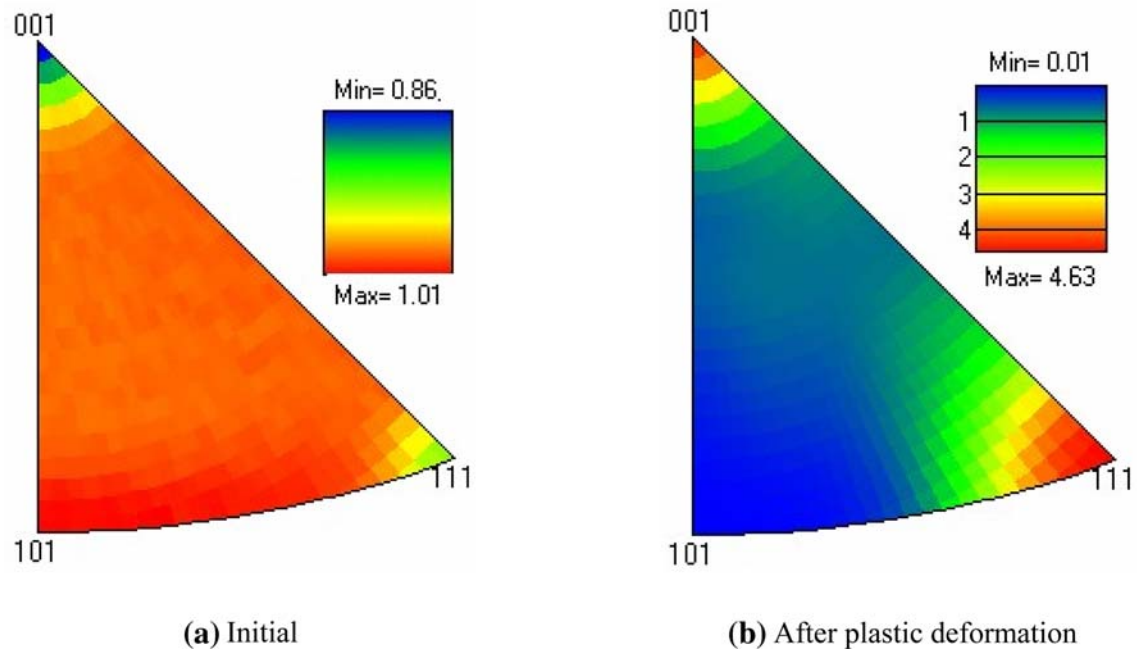


Fig. 4—The simulated inverse pole figures of the alloy in two different states: (a) initial texture within the elastic region and (b) after the onset of the plastic deformation at about 825 MPa of the stress-strain curve in Fig. 2.

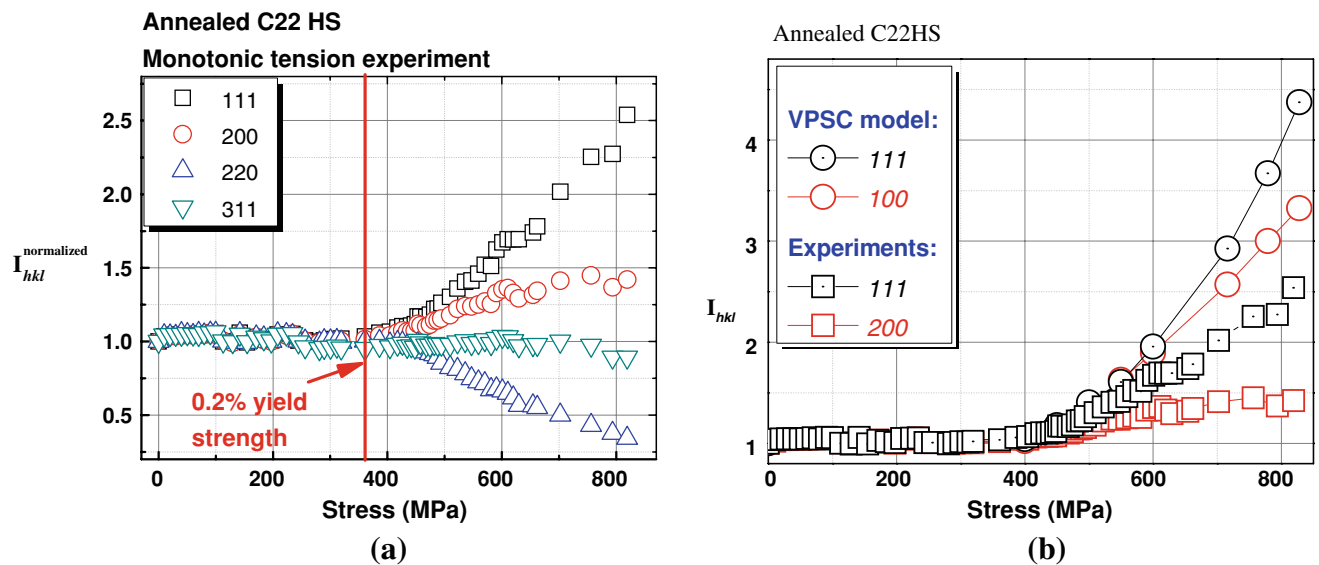


Fig. 5—(a) Normalized integrated intensity, using Eq. [2], vs true stress. For clarity, the data are plotted for the loading direction. The perpendicular red line represents the macroscopic 0.2 pct yield strength. (b) Simulated VPSC texture development along loading direction. There is a stronger texture in {111} pole than that of {100} pole, as measured in (a).

energy in the deformed specimen has been reported to generally derive from the randomly-distributed dislocations, the cellular-dislocation structure, and the heterogeneous elastic-energy contribution of the mean stresses.^[40–43] As a result, changes in the microstructures cause most of the observed peak broadening. To distinguish the physical contribution to broadening, Γ_{phys} , induced by the microstructure evolution, the

instrumental broadening, Γ_{ref} , needs to be taken into account. The value of Γ_{ref} was obtained by measuring the reference sample. The raw data, Γ_{Exper} , shown in Figures 6(a) and (b), were further adjusted to take into account the instrumental broadening ($\Gamma_{\text{phys}} = \Gamma_{\text{Exper}} - \Gamma_{\text{ref}}$). As a result, the physical broadening is more than half smaller than broadening of the raw experimental curves, Γ_{Exper} (Figure 6).

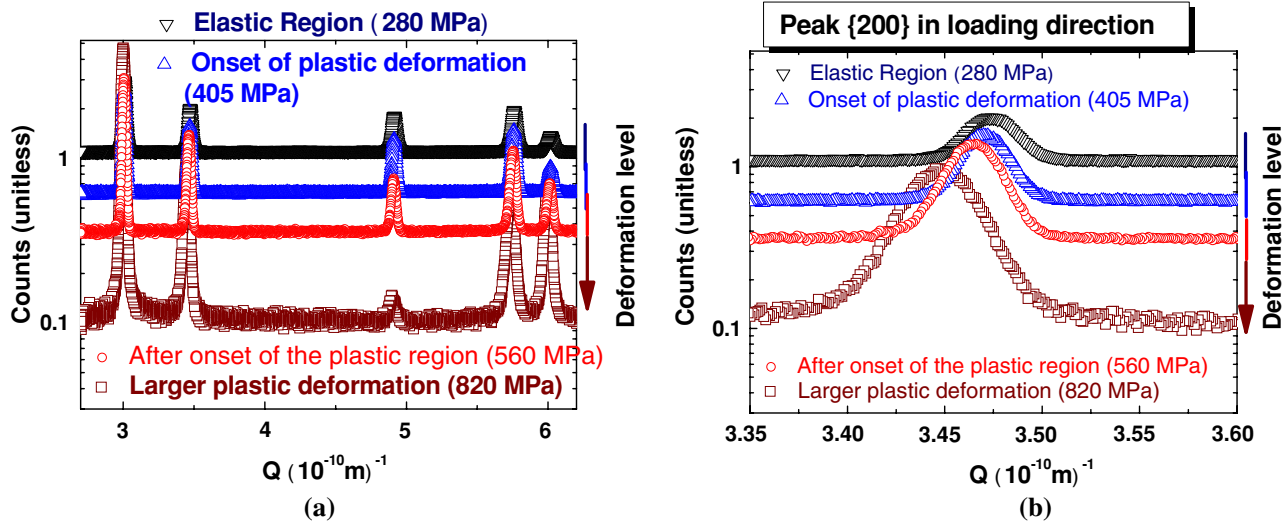


Fig. 6—(a) Selected diffraction profiles measured along the loading direction in a sequence from top to bottom at the stress: 280, 405, 560, and 820 MPa, respectively. (b) Enlargement of the peaks {200} from (a) different loading levels (raw data). There are clear changes in peak positions, intensities, and widths, where the sources of the peak-width broadening may come from the randomly distributed dislocations and dislocation walls. Note that the raw data in (a) and (b) include instrumental broadening, Γ_{ref} . For calculations of dislocation-structure parameters, the peak broadening was corrected to take into account the instrumental broadening. So the broadening induced from dislocation substructures can be refined. For example, the peak-broadening induced by dislocation-related structure is about 45 pct of the value shown in (b) for the larger plastic deformation (820 MPa).

It is known that the randomly distributed or weakly correlated dislocations yield the Gaussian peak broadening.^[27–29,44–46] The dislocation-wall structures, aggregated by the equidistant-edge dislocations, cause Lorentzian peak broadening.^[27–29] Such equidistant-dislocation walls result in local pairwise tilts between the two adjacent regions of the crystal. We note that stacking faults also result in Lorentzian-type broadening. However, stacking faults additionally cause distinct anisotropic shift of different (hkl) reflections, and their input can be separated from the one caused by equidistant-dislocation walls.^[45]

In the regions close to the boundaries at distances L , smaller than the distance, h , between the dislocations within the wall ($L < h$), the strain fields from individual dislocations forming the boundary become significant. This is extremely important for the detailed analyses based on the shape of the tails of the peak developed by Ungar *et al.*^[42] and Groma.^[47] Such analysis of the shape of the tails of diffraction peaks provides the most direct information about the dislocation density. However, the signal to noise at the tails of the neutron intensity profiles in our measurements was low and analysis of the shape of the tails could not be reliably used for the analysis of dislocation substructure. For this reason, in the present article, we used the central part of the peak broadening for the characterization of dislocation parameters, which depends mainly on displacement fields in the regions remote from the wall at the distances exceeding $L \gg h$.

For example, assuming a 10^{15} m^{-2} dislocation density of within the dislocation wall, the distance, h , between the dislocations within the wall becomes $h = 30 \text{ nm}$. This means that the strain fields appear in the diffraction profiles at values of $\Delta d^* \cong 0.03 \text{ nm}^{-1}$. In our experimental data, the region $\Delta d^* \cong 0.03 \text{ nm}^{-1}$ is located in the tails of the peak intensity and does not influence the central part of the peak, which was used for the analysis.

According to Balzar *et al.*,^[48,49] it is “generally accepted that a Voigt-function approximation for both size and strain broadened profiles is a better model than simplified integral-breadth methods.” A detailed description of the profile analysis for neutron TOF measurements is given in the GSAS manual.^[18,50] To distinguish these two broadening components, similar to the approach of Balzar *et al.*,^[48,49] the pseudo-Voigt function (Eq. [6]) is applied. It corresponds to the GSAS profile function 3.

$$V = \eta L + (1 - \eta)G \quad (0 \leq \eta \leq 1) \quad [6]$$

A parameter (η) is introduced as a variable proportion of pure Lorentzian (L) to pure Gaussian (G), where L and G are defined as Gaussian and Lorentzian peak widths in Eqs. [3] and [4], respectively. The pseudo-Voigt function is fit to each individual $\{hkl\}$ peaks to study these two sources of broadening by GSAS with Eq. [7]. A total of seven different (hkl) peaks were fitted. For better statistics, the results were then averaged over all measured (hkl) peaks.

$$\Gamma = \sqrt{\Gamma_g^5 + 2.69269\Gamma_g^4\gamma + 2.42843\Gamma_g^3\gamma^2 + 4.47163\Gamma_g^2\gamma^3 + 0.07842\Gamma_g\gamma^4 + \gamma^5} \quad [7]$$

The measured peak width (Γ) is composed by the Gaussian broadening (Γ_g), as shown in Eq. [8], and the Lorentzian broadening (Γ_L), as shown in Eq. [9].

$$\Gamma_g = \sqrt{8(\ln 2)\sigma^2} \quad [8]$$

$$\Gamma_L = \gamma \quad [9]$$

where σ and γ are the standard deviations of the Gaussian and Lorentzian profile components, respectively.

Based on the described model, the dislocation density (n) of the randomly distributed dislocations from each $\{hkl\}$ reflection can be estimated from the Gaussian peak-width component (ΔFWHM_G), which depends on the Burgers vector (\mathbf{b}), the contrast factor (C_r) for randomly distributed dislocations or dislocations with weak correlations, and the d_{hkl} spacing, as presented in Eq. [10].^[44–46]

$$n_{hkl} \sim \mathbf{b}d_{hkl} \frac{\Delta\text{FWHM}_G}{C_r} \quad [10]$$

The calculation of the contrast factors for the randomly-distributed portion of the dislocation population is performed using the formalism described in References 28, 29, and 44 through 46, and is similar to the method developed by the Ungar's Group.^[40–42]

The Lorentzian peak-broadening components (ΔFWHM_L) are used to calculate the equidistant-dislocation-wall spacing (D), as exhibited in Figure 6(d), with the contrast factor (C_{EW}) in Eq. [11].^[28,29,44–46]

$$D \sim \frac{\pi C_{EW}}{\Delta\text{FWHM}_L} \quad [11]$$

where C_{EW} is the contrast factor for the equidistant-edge-dislocation wall. Assuming all probable slip systems for the fcc materials equally activated, the total dislocation density, n , and the distance between the equidistant-dislocation-walls, D , were determined using Eqs. [10] and [11] (Figure 7). At the first approximation, the VPSC-simulated active slip systems are proportional to those of the measured dislocation structure evolution in Figure 7. The experimentally determined equidistant-dislocation-wall spacing is shown with hollow symbols: square (\square) for the loading and circle (\circ) for the transverse directions, respectively. The dislocation density is presented in solid symbols, square (\blacksquare) for the loading direction and circle (\bullet) for the transverse direction. The dislocation density changes slowly within the 0 to 370 MPa elastic region. With the onset of the plastic deformation, the dislocation density starts to increase. The dislocation density slowly saturates after 870 MPa, but the equidistant-dislocation-wall spacing keeps decreasing to the final measurement. The current results, shown in Figure 7, are qualitatively similar to the previous calculations, with the assumption of the equal-dislocation activity from all primary slip systems.^[51] Complementary TEM analysis confirms the formation of the hierarchical dislocation structure with part of the dislocations grouped within the walls and part remaining randomly distributed between them (Figure 8). Both images in Figure 8 are taken from the

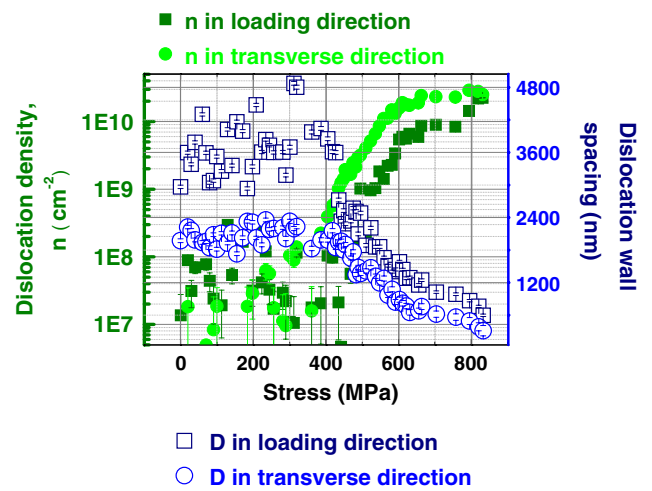


Fig. 7—Trends of the dislocation-wall spacing evolution (\square in loading direction and \circ in transverse direction) and density evolution (\blacksquare in loading direction and \bullet in transverse direction).

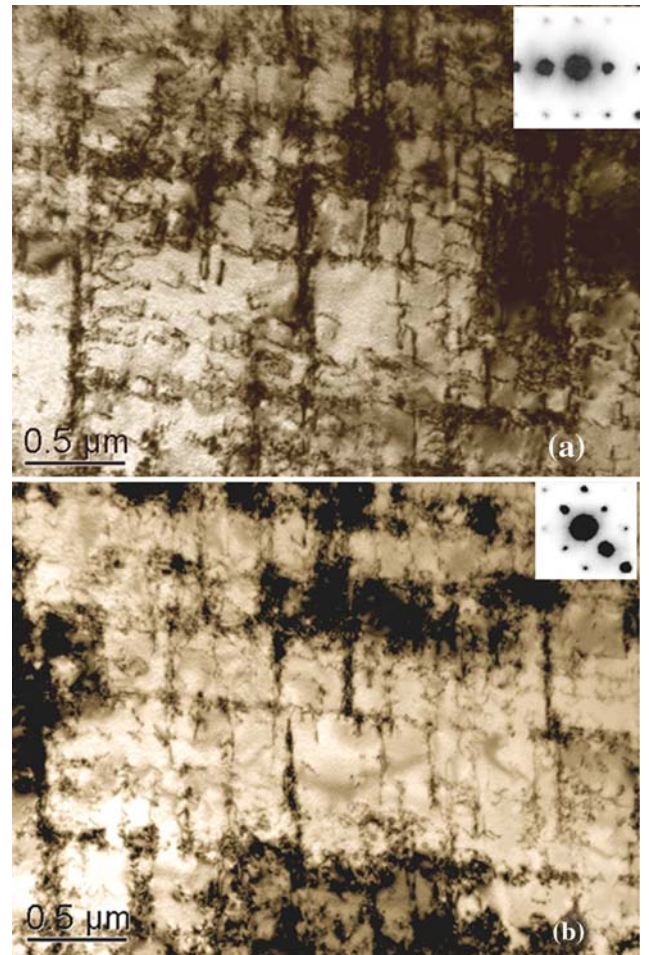


Fig. 8—TEM images obtained from the sample after 40 pct deformation demonstrate formation of the hierarchical dislocation structure with walls and some part of random dislocations between them: (a) diffraction vector $\mathbf{g} = [111]$, electron beam direction, B, near $[112]$; and (b) $\mathbf{g} = [200]$, B near (001), foil normal near (001). Due to different orientations of the diffraction vector, some dislocations become invisible at one of the images. Note that the dislocation walls are $\{110\}$ and are not aligned on $\{001\}$.

same area of the sample deformed at 40 pct, but at different diffraction vectors, \mathbf{g} . Diffraction at two different \mathbf{g} vectors changes invisibility conditions for some dislocations. For this reason, some of the dislocations are visible only at one of the images. Some dislocation debris is visible between the walls. The “blocky” structure showed typical dimensions of less than $0.5\ \mu\text{m}$. The walls are aligned along $\{110\}$ not $\{100\}$. The distance between the walls estimated from the TEM data is surprisingly close to the average data obtained from neutron diffraction.

Motivated by Heidelberg’s comments^[1] and based on the preceding experimental results, an attempt to track the microstructure of the single grains inside a polycrystal during deformation is discussed.

IV. DISCUSSION

The lattice strain-stress relationships measured from seven different $\{hkl\}$ planes shown in Figure 2 demonstrate a clear linear response within the elastic region, especially below 300 MPa. Beyond the 0.2 pct yield strength, the slope of the stiffest $\{111\}$ direction becomes smaller due to load sharing with the other grain orientation. The peak-intensity evolution in Figure 5(a) shows a clear onset of texture development, once the alloy was plastically deformed beyond the 0.2 pct yield strength. Note that the input of the simulation is based on our measured data: The comparison between the experimental measurement and the simulated results is based on the macrostress-macrostrain curve (Figure 3) and the lattice-strain evolution along the loading direction (Figure 9), respectively. The measured stress-strain

points are located on the simulated stress-strain curve from 0 to 20 pct strain. The simulated and experimental results practically coincide for strains up to 25 pct. At higher strains, the simulation gives slightly larger stress values than those measured. For the lattice-strain comparison, it can be seen that the VPSC simulations capture the characteristics of the lattice-strain distribution for most $\{hkl\}$ within 370 MPa in the elastic region. It also shows the different slopes of each $\{hkl\}$ corresponding to the respective elastic modulus according to the generalized Hooke’s law. The measured $\{111\}$ and $\{220\}$ lattice-strain evolution is practically reproduced from the simulation. The deviation of the slopes is found on the $\{200\}$ and $\{311\}$, which may be attributed to the hardening parameters influenced by the microstructure.

Based on the preceding comparison and the agreement of the texture development from the measured and the simulated results, the simulated slip-system activity could be used for calculating the dislocation-contrast factor. Moreover, since the simulated grains contain the information of the grain orientation, single grains with specific orientations can be selected.

The reason to select the specifically oriented grains is to consider the specimen-coordinate system confined by the setup of the two-directional detection banks during the *in-situ* measurements. Figure 10 shows the details of this consideration. The specimen geometry is shown at the top of Figure 10. The incident beam can be diffracted in several directions. Only diffraction from grains along the loading (in black arrow) and transverse (in red arrow) directions can be collected from the detection banks. However, during the plastic deformation, the grains can rotate their local grain-coordinate system, as shown in the bottom-left of Figure 10. The responses of these materials, as grains rotate, can be measured only when these grains are reoriented into aligned planes in the loading and transverse directions of the specimen (Figure 10).

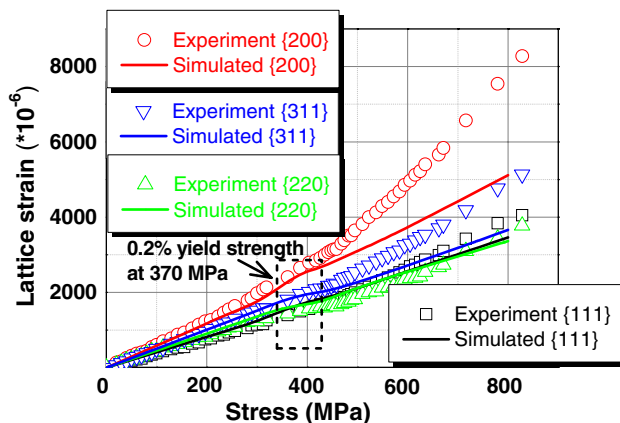


Fig. 9—Response of the measured (symbols) and the simulated (lines) lattice strains to the load along the loading direction for $\{111\}$ in \blacksquare , $\{200\}$ in \bullet , $\{220\}$ in \blacktriangle , and $\{311\}$ in \blacktriangledown . The simulated and the experimental results show qualitative equivalence as the $\{200\}$ in \bullet increases fastest while the $\{110\}$ in \blacksquare increases the least. Quantitatively, the simulation and the measurements almost match correspondingly to stress up to 370 MPa. However, the simulated lines start to show less lattice-strain responses deviated from the measured data about 400 MPa. Although the qualitative trends remain the same from the simulated to the measured, the simulated $\{200\}$ lattice strain is about $2500\ \mu\epsilon$ less than that of the measured strain at stress equal to 800 MPa.

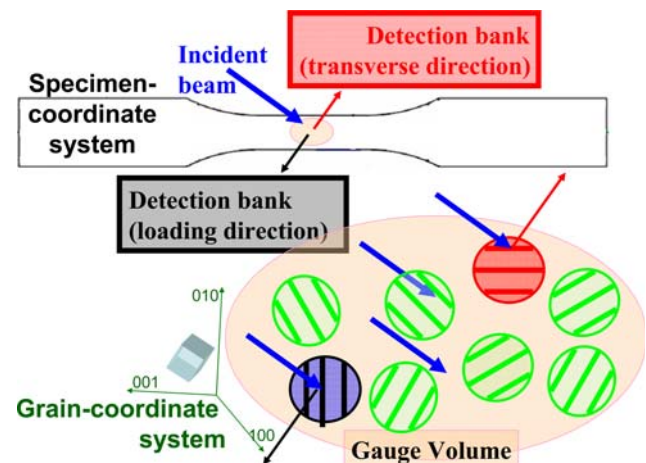


Fig. 10—Simulated grains reorient after deformation as the grain-orientation system (bottom-left). Only the specifically oriented grains are assumed to be measured at a specific part of the Debye ring from the gage volume (bottom-right). The directions are based on the specimen-coordinate system, fixed by two detection banks, as shown on top.

Table III. Probability of the Active Slip System $\{hkl\}$ $\langle uvw \rangle$ of the Grains That Could Diffract to the Detection Banks

Grain Oriented to the Loading Direction						
h	k	l	u	v	w	Probability
1	1	1	0	1	$\bar{1}$	7.60 pct
$\bar{1}$	1	1	1	0	$\bar{1}$	24.14 pct
$\bar{1}$	1	1	1	0	1	33.28 pct
1	1	$\bar{1}$	0	1	1	14.69 pct
1	$\bar{1}$	1	0	1	1	8.49 pct
Grain Oriented to the Transverse Direction						
h	k	l	u	v	w	Probability
1	1	1	0	1	$\bar{1}$	0.81 pct
$\bar{1}$	1	1	1	0	$\bar{1}$	29.20 pct
$\bar{1}$	1	1	0	1	$\bar{1}$	6.37 pct
$\bar{1}$	1	1	1	0	1	40.14 pct
1	1	$\bar{1}$	0	1	1	23.48 pct

As a result, a search of the simulated grains is based on the relative orientation of the grains with respect to the specimen-coordinate system. Although there are only a few grains oriented along these two directions, the grains that do reorient to the detector directions can be used to study the slip-system evolution in these specifically oriented grains embedded within our 2592-grain, polycrystalline models. The simulated slip-system activity is shown in Table III.

From the 2592 grains used in the simulation, only two grains are favorably oriented to diffract in the direction of detection banks (Table III). The first grain is nearly exactly oriented for diffraction into both banks. The accumulated probability for the two most favorable slip systems in the loading direction is approximately 57 pct, and the accumulated probability with an additional slip system is approximately 72 pct. In a second grain, favorably oriented for diffraction in the transverse direction, we also observe that the accumulated probability for three slip systems reaches 92 pct. The results suggest that the number of active slip systems with the probability (from 15 to 40 pct) for different grains is between 2 and 3. This result agrees with Fleischer's^[52] TEM investigation of brass crystals, showing that the average number of active slip planes is about 2.5. If slip systems with a 5 to 15 pct probability are included, about five systems are predicted by the model. This is in an agreement with the observations of Margulies *et al.*^[53]

For most probable slip systems, the slip-system-dependent contrast factors were calculated (Table III) for the grain with best orientation for diffraction into each detection bank (Figure 10). The parameters of dislocation arrangements calculated based on Eqs. [10] and [11] are presented in Table IV. The estimated dislocation density and dislocation-wall spacing obtained from the loading and the transverse directions are essentially the same (Table IV) and agree with TEM observations.

Table IV. Slip-System-Dependent Contrast Factor, Screw-Dislocation Density (n), Edge-Dislocation-Wall Spacing (D) of the Specifically Oriented Grain in the Loading Direction at 825 MPa

b_i	Detection-Bank Directions	Contrast Factor		n (10^8 cm^{-2})	D (nm)
		Edge Wall	Random Screw		
[100]	loading	0.27	0.19	142 (± 1.5)	785 (± 16)
[010]	transverse	0.25	0.18	148 (± 1.6)	762 (± 15)

As a result, our method demonstrates a new approach to the study of microstructure evolution during tension. Overall, the results are used to understand the slip-system-related microstructure evolution during tensile deformation. There is a good agreement between simulated and experimental results because the dominant deformation mechanism of the alloy is the slip activity, which is the fundamental assumption in our VPSC model. In the future, this method will be applied to other cubic materials.

V. CONCLUSIONS

The present study reports combined effects of experiments and simulations of plastic deformation in an fcc nickel-based single-phase superalloy under tension. Texture simulations beyond 30 pct deformation with the VPSC model were performed. The simulations were based on the lattice strains measured by *in-situ* neutron-diffraction experiments at room temperature during tension experiments. The preferred orientations were simulated for the ensemble of 2592 grains. The gradual development of the texture is both simulated and measured by *in-situ* neutron experiments. The agreement between the experimental measurements and simulated results demonstrates that the assumed crystallographic slip systems are the major contributors during plastic deformation of the superalloy. A possible contribution of each grain into the Debye diffraction-intensity ring was determined, and the two grains with the specific orientation diffracting neutrons in the directions of two detection banks were found. For the preceding two grains, the dislocation-contrast factor has been updated with the simulated probability of the active slip systems. The slip-system-dependent contrast factors are used to calculate the parameters of the dislocation arrangement for the specifically oriented grains.

ACKNOWLEDGMENTS

This research is supported by the National Science Foundation (NSF), International Materials Institutes (IMI) Program (Grant No. DMR-0231320), and the National Natural Science Foundation (NNSF) of China (Grant No. 50671022). This research was sponsored by the Division of Materials Science and Engineering,

Office of Basic Energy Science, United States Department of Energy, under Contract No. DE-AC05-00OR22725 with UT-Battelle, LLC. The Lujan Neutron Scattering Center at LANSCE is funded by the Department of Energy's Office of Basic Energy Science. The Los Alamos National Laboratory is operated by the Los Alamos National Security LLC under DOE Contract No. DE-AC52-06NA25396. The alloys are supported by Haynes International Inc., from Drs. Dwaine L. Klarstrom and Lee M. Pike. The authors appreciate the discussions with Dr. Michael L. Benson, Nuclear Regulation Council (NRC).

REFERENCES

1. F. Heidebach: *Science*, 2001, vol. 291, pp. 2330–31.
2. N. Hansen: *Metall. Mater. Trans. A*, 2001, vol. 32A, pp. 2917–35.
3. R. Hill: *J. Mech. Phys. Solids*, 1965, vol. 13, pp. 89–101.
4. J.W. Hutchinson: *Proc. R. Soc. London A*, 1970, vol. 319, pp. 247–72.
5. T. Holden, C.N. Tome, and R.A. Holt: *Metall. Mater. Trans. A*, 1998, vol. 29A, pp. 2967–73.
6. B. Clausen, T. Lorentzen, M.A.M. Bourke, and M.R. Daymond: *Mater. Sci. Eng. A*, 1999, vol. 259, pp. 17–24.
7. B. Clausen, T. Lorentzen, and T. Leffers: *Acta Mater.*, 1998, vol. 46, pp. 3087–98.
8. J.W.L. Pang, T.M. Holden, J.S. Wright, and T.E. Mason: *Acta Mater.*, 2000, vol. 48, pp. 1131–40.
9. M.R. Daymond, M. Preuss, and B. Clausen: *Acta Mater.*, 2007, vol. 55, pp. 3089–102.
10. M.R. Daymond, C.N. Tome, and M.A.M. Bourke: *Acta Mater.*, 2000, vol. 48, pp. 553–64.
11. U.F. Kocks, C.N. Tome, and H.-R. Wenk: *Texture and Anisotropy: Preferred Orientation in Polycrystals and Their Effects on Materials Properties*, Cambridge University Press, Cambridge, United Kingdom, 1998, vol. 1, pp. 466–78.
12. Y.D. Wang, X.-L. Wang, A.D. Stoica, J.D. Almer, U. Lienert, and D.R. Haeflner: *J. Appl. Cryst.*, 2002, vol. 35, pp. 684–88.
13. Y.D. Wang, R.L. Peng, and R.L. McGreevy: *Phil. Mag. Lett.*, 2001, vol. 81, pp. 153–63.
14. Y.D. Wang, R.L. Peng, J.D. Almer, M. Oden, Y.D. Liu, J.N. Deng, C.S. He, Q.L. Li, and L. Zuo: *Adv. Mater.*, 2005, vol. 17, pp. 1221–26.
15. E.-W. Huang, B. Clausen, Y.D. Wang, H. Choo, P.K. Liaw, M.L. Benson, L.M. Pike, and D.L. Klarstrom: *Int. J. Fatigue*, 2007, vol. 29, pp. 1812–19.
16. Y.L. Lu, L.M. Pike, C.R. Brooks, P.K. Liaw, and D.L. Klarstrom: *Scripta Mater.*, 2007, vol. 56, pp. 121–24.
17. M.A.M. Bourke, D.C. Dunand, and E. Ustundag: *Appl. Phys. A*, 2002, vol. 74, pp. 1707–09.
18. R.B. Von Dreele: *J. Appl. Cryst.*, 1982, vol. 15, pp. 581–89.
19. H. Mughrabi: *Acta Metall.*, 1983, vol. 31, pp. 1367–79.
20. L. Levine, B.C. Larson, W. Yang, M.E. Kassner, J.Z. Tischler, M.A. Delos-Reyes, R.J. Fields, and W. Liu: *Nat. Mater.*, 2006, vol. 5, pp. 619–22.
21. D. Kuhlmann-Wilsdorf: *Philos. Mag. A*, 1999, vol. 79, pp. 955–1008.
22. N. Hansen: *Adv. Eng. Mater.*, 2005, vol. 7, pp. 815–21.
23. W.D. Nix, J.C. Gibeling, and D.A. Hughes: *Metall. Trans. A*, 1985, vol. 16A, pp. 2215–26.
24. M. Zehetbauer: *Acta Metall. Mater.*, 1993, vol. 41, pp. 589–99.
25. E. Schaffer, K. Simon, S. Bernstorff, P. Hanak, G. Tichy, T. Ungar, and M.J. Zehetbauer: *Acta Mater.*, 2005, vol. 53, pp. 315–22.
26. D.A. Hughes and N. Hansen: *Metall. Trans. A*, 1993, vol. 24A, pp. 2021–37.
27. M.A. Krivoglaz, K.P. Ryaboshapka, and R.I. Barabash: *Phys. Met. Metallogr.*, 1970, vol. 30, pp. 1134–45.
28. R.I. Barabash and P. Klimanek: *J. Appl. Cryst.*, 1999, vol. 32, pp. 1050–59.
29. R.I. Barabash, G.E. Ice, and F. Walker: *J. Appl. Phys.*, 2003, vol. 93, pp. 1457–64.
30. W.T. Read and W. Shockley: *Phys. Rev.*, 1950, vol. 78, pp. 275–89.
31. R.W. Hertzberg: *Deformation and Fracture Mechanics of Engineering Materials*, 2nd ed., John Wiley & Sons, Inc., New York, NY, 1983, pp. 9–16.
32. J.W. Hutchinson: *Proc. R. Soc. London A*, 1976, vol. 348, pp. 101–27.
33. R.A. Lebensohn and C.N. Tome: *Acta Metall. Mater.*, 1993, vol. 41, pp. 2611–24.
34. N. Jia, R.L. Peng, Y.D. Wang, S. Johansson, and P.K. Liaw: *Acta Mater.*, 2008, vol. 56, pp. 782–93.
35. A. Baczmanski and C. Braham: *Acta Mater.*, 2004, vol. 52, pp. 1133–42.
36. P. Haasen: *Physical Metallurgy*, Cambridge University Press, Cambridge, United Kingdom, 1996, pp. 285–326.
37. H.-R. Wenk and S. Grigull: *J. Appl. Cryst.*, 2003, vol. 36, pp. 1040–49.
38. Q. Liu, D.J. Jensen, and N. Hansen: *Acta Mater.*, 1998, vol. 46, pp. 5819–38.
39. G.I. Taylor: *J. Inst. Mater.*, 1938, vol. 62, pp. 307–24.
40. H. Biermann, T. Ungar, T. Pfannenmuller, G. Hofmann, A. Borbely, and H. Mughrabi: *Acta Metall.*, 1993, vol. 41, pp. 2743–53.
41. A. Borbely, J.H. Driver, and T. Ungar: *Acta Mater.*, 2000, vol. 48, pp. 2005–16.
42. T. Ungar, I. Groma, and M. Wilkens: *J. Appl. Cryst.*, 1989, vol. 22, pp. 26–34.
43. G. Will: *Powder Diffraction: The Rietveld Method and The Two-Stage Method*, 1st ed., Springer, Berlin, 2006, ch. 1, pp. 37–39.
44. R.I. Barabash and M.A. Krivoglaz: *Metallofizika*, 1982, vol. 4, pp. 3–10.
45. M.A. Krivoglaz: *X-Ray and Neutron Diffraction in Nonideal Crystal*, 1st ed., Springer, Berlin, 1996, pp. 465–67.
46. M.A. Krivoglaz: *Theory of X-Ray and Thermal Neutron Scattering by Real Crystals*, 1st ed., Plenum, New York, NY, 1969, pp. 405–15.
47. I. Groma: *Phys. Rev. B*, 1998, vol. 57, pp. 7535–42.
48. D. Balzar, N. Audebrand, M.R. Daymond, A. Fitch, A. Hewat, J.I. Langford, A. Le Bail, D. Louer, O. Masson, C.N. McCowan, N.C. Popa, P.W. Stephens, and B.H. Toby: *J. Appl. Cryst.*, 2004, vol. 37, pp. 911–24.
49. D. Balzar and H. Ledbetter: *J. Appl. Cryst.*, 1993, vol. 26, pp. 97–103.
50. A.C. Larson and R.B. Von Dreele: *General Structure Analysis System GSAS*, Los Alamos National Laboratory Report, Los Alamos, NM, 2001, pp. 147–167.
51. E.-W. Huang, R.I. Barabash, Y. Wang, B. Clausen, L. Li, P.K. Liaw, G.E. Ice, Y. Ren, H. Choo, L.M. Pike, and D.L. Klarstrom: *Int. J. Plast.*, 2008, vol. 24 (08), pp. 1440–56.
52. R.L. Fleischer: *Acta Metall.*, 1987, vol. 35, pp. 2129–36.
53. L. Margulies, G. Winther, and H.F. Poulsen: *Science*, 2001, vol. 291, pp. 2392–94.